4 Experimental details

This chapter is devoted to the description of the experimental setup involved in the present work, which consists mainly of two parts:

1. the ultra-high vacuum (UHV) chamber

2. the femtosecond laser system

The UHV chamber is used for the preparation and characterization of thin films, and also for the optical measurements. The femtosecond laser is the light source, providing ultrashort and high energy pulses necessary for the steady-state and time-resolved linear and nonlinear optical spectroscopy.
In the following, the experimental devices together with the employed measurement techniques, the second harmonic generation (SHG) and the linear reflectivity (LR), will be presented.

4.1 UHV chamber

Accounting for the high reactivity exhibited by rare-earth elements, and in particular by gadolinium, an ultra-high vacuum environment is necessary for the preparation of high quality rare-earth thin films. Generally, ultra-low pressures are obtainable after a careful bake-out of the UHV vessel and additional chemical pumping using *e.g.* ion-getter pumps and/or titanium sublimation pumps. In this way pressures in the 10^{-11}mbar range are achievable. The UHV chamber used in this work - depicted in figure 4.1 - is pumped by a turbomolecular pump (Leybold Turbovac 361) together with a pumping stage (Pfeiffer) consisting of a turbomolecular pump and a diaphragm pump, the latter one serving as a pre-vacuum pump. In order to get lower pressures, a titanium sublimation pump (TSP) is employed. In this context the high reactivity of gadolinium is very useful since one can utilize it as an additional modality of chemical pumping. By combining its effect with the TSP pumping, the achieved base pressure is around $2x10^{-11}$mbar. The residual gas analysis of the obtained vacuum is performed with a quadrupole mass spectrometer (QMS). The QMS is also used as a detector for the desorbed species in the temperature desorption spectroscopy (TDS) measurements.

The UHV chamber, sketched in the figure 4.1, is structured on two levels: the *preparation level* for thin film deposition and characterization and the *optical level* for the linear and nonlinear optical measurements. In the preparation level three home-build evaporators are installed, which provide us with enough provisions of gadolinium (Gd), yttrium (Y) and terbium (Tb). Thin films of these materials are prepared by electron-beam evaporation from tungsten (W) crucibles with the film thickness and deposition rate being monitored by a quartz microbalance (QMB). For checking the morphology and the long-range structural
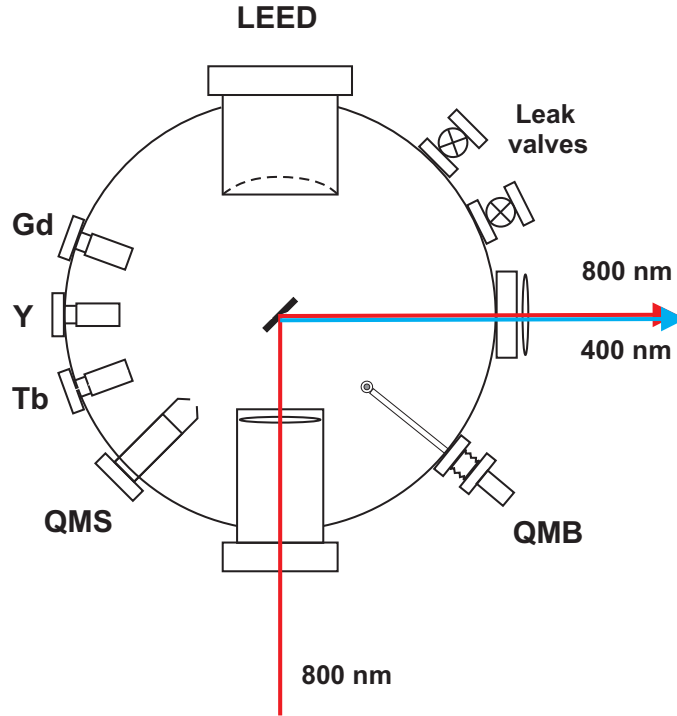
Figure 4.1: Schematic picture of the UHV chamber. The Gd, Y, and Tb evaporators together with the quartz microbalance (QMB), the quadrupole mass spectrometer (QMS) and the low energy electron diffraction (LEED) device are situated in the preparation level. The special designed flange with the lenses for focussing and collimating the laser beams (the displayed fundamental and the second harmonic wavelengths are typically 800 nm and 400 nm, respectively) are in the optical level. Also the leak valves for dosing xenon and oxygen are depicted.

ordering of the deposited films and also for the substrate quality, a low electron energy diffraction (LEED) device is used. A pair of leak valves are utilized to dose xenon (Xe) and oxygen (O_2) in UHV.

For the optical level, a special entrance flange has been designed, allowing the positioning of the focusing lens closer to the sample. Hence a better focus of the laser beam is achieved (diameter in focus $\approx 70 \mu m$), that results in higher laser fluences[1](typical $\approx 1 \mathrm{mJ/cm^2}$). Fused silica UHV windows were used for entrance and exit of laser beams, a material exhibiting high transmission ($\geq 95\%$) over a wide spectral range (250 nm to 2 μm). Also, an electromagnet (not shown) is installed, producing magnetic fields up to 500 Gauss, which is sufficient to magnetize the films in saturation along the easy axis.
The sample holder is attached to the cold finger of a continuous flow cryostat, which can be used either with liquid nitrogen or liquid helium. The whole construction is mounted on a differentially pumped manipulator that allows displacements along x, y, and z axis (vertical) as well as 360° rotation.

---

[1]The laser fluence is defined as the ratio $\frac{E_p}{A}$, where E_p is the energy per pulse in mJ and A is the laser illuminated area in cm^2.
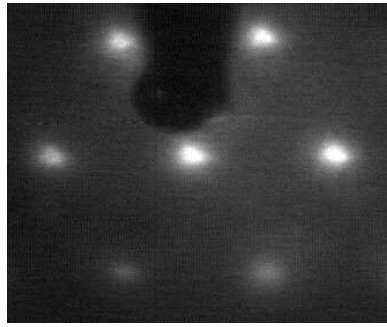
Figure 4.2: LEED pattern from a 10 nm Gd(0001)/W(110) film deposited at room temperature and annealed to 680 K for 10 min. The LEED picture is recorded at a beam energy of 218 eV and at a sample temperature of 100 K.

4.1.1 Sample preparation

Both materials investigated in this work, Gd and Y, have been grown on a tungsten(110) substrate. Since we have used a similar preparation procedure for the Gd(0001) and Y(0001) thin films, we focus in the following on the Gd(0001)/W(110), being the most investigated system in this work.

Growing of rare earth metals on refractory materials substrates like W(110) (also Mo(110)), presents several advantages that makes this substrate very feasible in preparing high quality rare-earth thin films. One of the reasons is the high surface energy of the W surface that favors a layer-by-layer type of growth and the fact that the deposited material does not form alloys with the substrate. Also the bcc(110) surface is atomically smooth that results in a high mobility of the adsorbed atoms. Moreover, there is a relatively good matching between the support substrate and the deposited film, with a lattice mismatch for the Gd(0001)/W(110) system that amounts to $\approx$15%. This causes a Gd lattice distortion that becomes weaker and disappears by strain release after 4 monolayers (ML) of Gd(0001) film [24]. Furthermore, this substrate is paramagnetic having no influence on magnetic properties of the deposited overlayer. Cleaning the substrate can be performed in a easy manner and is not a time consuming procedure in comparison with sputtering+annealing cycles, that are necessary for other systems *e.g.* Ni/Cu(001). From technical point of view this constitutes a major advantage.

One necessary condition for a good quality of deposited film is that the substrate is clean, showing no impurities. The W(110) substrate is cleaned by short (several seconds) cycles of heating up to $\approx$2600 K, a process known as flashing. The usual contaminants, which diffuse from the bulk upon heating, are carbon and sulfur. These can be removed after several cycles of heating the sample to $\approx$1600 K in partial pressure of oxygen (p = 2×10^{-7}mbar). During this procedure the contaminants are oxidized and desorbed. For a clean substrate an additional cycle of flashing is required in order to remove the more stable tungsten oxides. Normally, the above mentioned procedure should be repeated after the preparation of 30 to 40 films, as has been done in the present work.

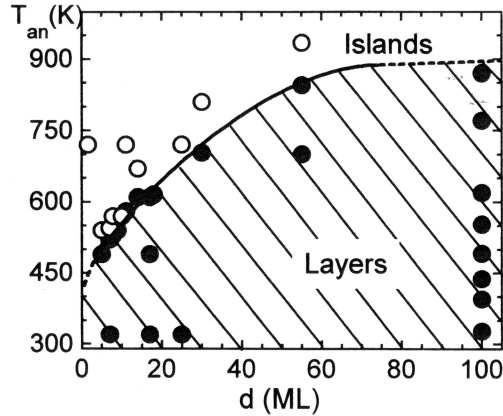As mentioned above, gadolinium grows epitaxially on W(110) in a layer-by-layer mode

Figure 4.3: The dependence of the Gd(0001) films morphology on the annealing temperatures for various film thicknesses, as was measured with ac susceptibility by Aspelmaier *et al.* [121]. One can obtain 3D islands or 2D films by choosing the appropriate annealing temperature. Taken from [122].

(Frank-van der Merwe mode) [122, 33] owing to the bigger free energy of tungsten surface, which favors a two-dimensional (2D) type of growth. After a short annealing cycle, the film acquires a long range crystalline order. This is illustrated in the figure 4.2, where the LEED pattern from a 10 nm Gd(0001) film annealed to 680 K is shown. Making use of even higher annealing temperatures the film morphology changes to a Stranky-Krastranov mode *i.e.* three-dimensional (3D) islands on top of a flat film [123]. In the present work, a relatively similar procedure in growing thin gadolinium films on W(110) substrate has been used, as was described by Aspelmaier *et al.* [121]. They performed a thorough study of critical annealing temperatures for Gd films with different thicknesses, at which the transformation from a 2D film to 3D islands takes place. Their results are shown in the figure 4.3.

Our daily used recipe in growing thick gadolinium films is as follows: a 20 nm (the typical thickness) gadolinium film is deposited on the tungsten substrate held at room temperature, at a deposition rate of $\sim$ 6 Å/min followed by 10 min annealing to 680 K. This produces a smooth and well ordered film, which can be judged from the LEED picture shown in the figure 4.2.

Before we end the section regarding the sample preparation, is worthwhile mentioning how the residual gases of the UHV environment can influence the surface quality of the prepared rare-earth films and what is special for our case. Even for base pressures in the 10^{-11} mbar range a freshly prepared film will be covered by a layer of adsorbed residual gas molecules in a time interval of $\approx$ 3-4 hours, accounting for the definition of one langmuir 1 L=10^{-6}torr·s. Upon adsorption of various residual gases the surface electronic structure is significantly affected. For the case of Gd(0001) surface, the exchange-split surface state (see chapter 2) can be used as an indicator for the cleanliness of the surface. Photoemission measurements on Gd(0001) use the signal arising from the surface state as a signature for the surface quality [124] and report a degradation and a subsequent disappearance of the
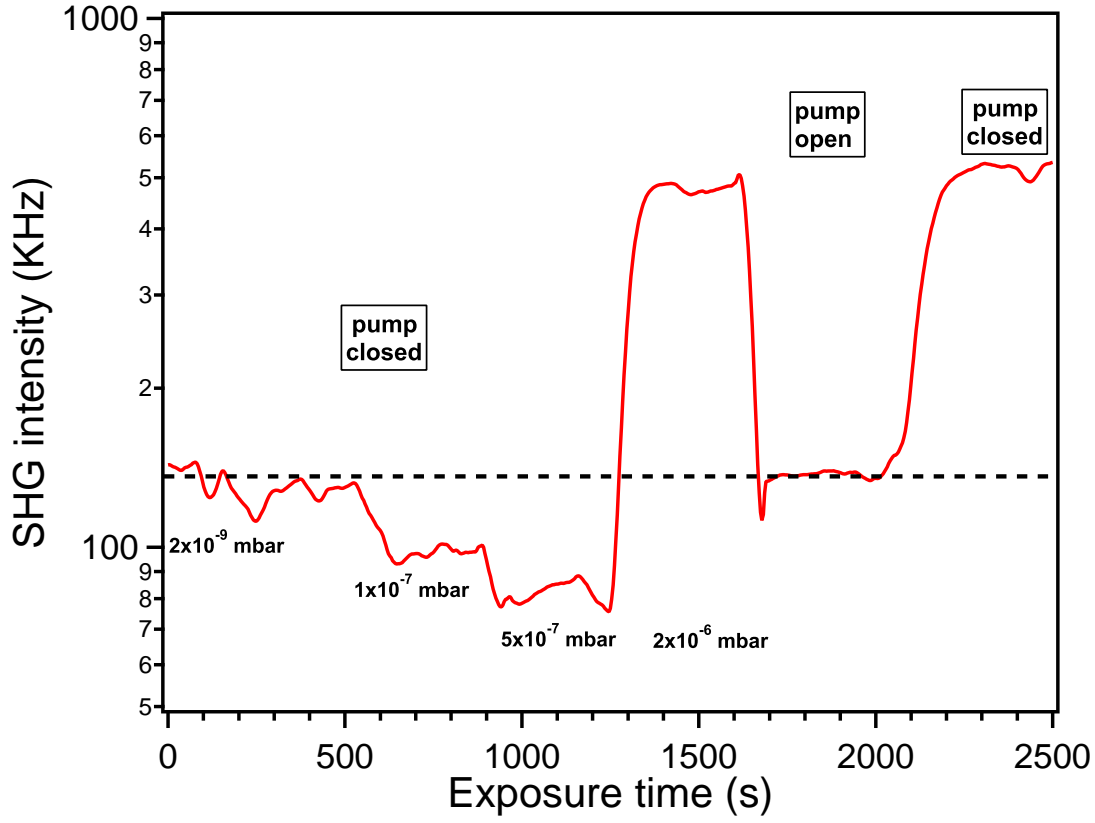
Figure 4.4: The variation of the SHG signal (of the probe beam) with the H_2 exposure for a sequential opening and closing of the pump beam. The pump and probe beams are spatially and temporally overlapped. During the measurement the sample is continuously exposed to H_2 at various partial pressures. Note the logarithmic scale of the y axis.

surface state signal after a few hours with a vacuum in the 10^{-11} mbar range [125]. Since the surface quality is of utmost importance for us, we have performed a test measurement by exposing a freshly prepared Gd(0001) film to molecular hydrogen at various partial pressures. Simultaneously we monitor the SHG signal, that arises mainly from the surface state (see chapters 3 and 5). The result is plotted in the figure 4.4, where the SHG yield (from the probe beam) is displayed for open and closed pump beam (more intense than the probe beam - see section 4.3). We observe initially for a closed pump a decrease of the SHG signal with step-like features, that corresponds to different exposure pressures of H_2: from $2 \cdot 10^{-9}$mbar to $5 \cdot 10^{-7}$ mbar. This indicates a degradation of the surface quality by the H_2 adsorption. A sharp increase of the SHG yield (almost one order of magnitude) appears for a H_2 partial pressure of $2 \cdot 10^{-6}$mbar, that might indicate a SHG resonance enhancement via an adsorbate electronic state. When the pump is open a sudden decrease of the SHG yield to the initial level, before adsorption, is noticed. The sequence is repeated and the same level of SHG signal are detected for the open and close pump. Therefore we can conclude that we produce a very efficient laser-induced cleaning

of the surface based on the laser-induced desorption process. We have to keep in mind that for the real measurements the residual gases are at much lower concentrations than the exposures used here. This result is corroborated by the features of the time-resolved measurements, which were showing a similar quality even for films that were four days old.

4.1.2 Sample holder

Along this work two different types of sample holder were used: one which was optimized for photoemission measurements, but having the drawback of low cooling efficiencies (used in earlier stage of the present work), and the second one being an improved version in terms of robustness and cooling. For comparison both sample holders are sketched in the figure 4.5.

The fundamental difference between them, rely on sample mounting: while in the first case the tungsten crystal is mounted between a W stick and a W wire, for the second variant the crystal is actually wrapped by the tungsten wires. Hence, the thermal contact is different: for the first variant the contact with the cooling reservoir is done just through the sharpened W stick via the tantalum block and the Ta screw, whereas for the second variant, a better thermal contact is realized between the cooling source and the sample via the W wires and Cu legs. Therefore, the latter solution provides an extended contact surface between sample and the cooling reservoir, which increased significantly the efficiency of cooling (cooling the sample with liquid helium, 20 K could be achieved with the improved version whereas just 60-70 K with the old version). In the following the second variant of the sample holder is described.

The W(110) crystal is mounted with the help of two tungsten wires (diameter 0.3 mm), which are wrapped around and tightly fixed on the sample holder legs. This is done by pressing the W wires between a 1 mm thick tantalum plate and the sample holder leg. The copper legs are covered with a thin tantalum foil as a safety precaution in order to prevent any damage, which can be produced during flashing. Electrical isolation and good thermal conductivity at low temperatures, are ensured by employing a pair of sapphire plates (thickness 1 mm), which are mounted between the main rod and the Cu legs. The sapphire plates are polished in order to provide a better contact with the main rod and the holder legs. A protective Cu shield (not shown) is mounted in order to hinder the deposition of metal films on the sapphire plates during flashing. By this, the appearance of electrical short-circuits is avoided.

The sample holder components are made of high purity copper and are gold-coated to reflect the thermal radiation. This latter fact together with a radiation shield (mentioned above) made of Cu, that is mounted concentric around the sample holder, assure a good cooling efficiency in the low temperatures range. The entire construction is attached to the cryostat coldfinger, which is used mainly with liquid helium. With this type of sample holder the lowest achieved temperature is around 20 K. Heating of the sample can be done in two ways: either by resistive heating via the tungsten wires which hold the sample or by electron bombardment using the a tantalum filament (diameter 0.3 mm) installed behind the sample. The filament has a spiral-like shape in order to produce a spatially homogeneous heating of the W sample. For direct heating currents between
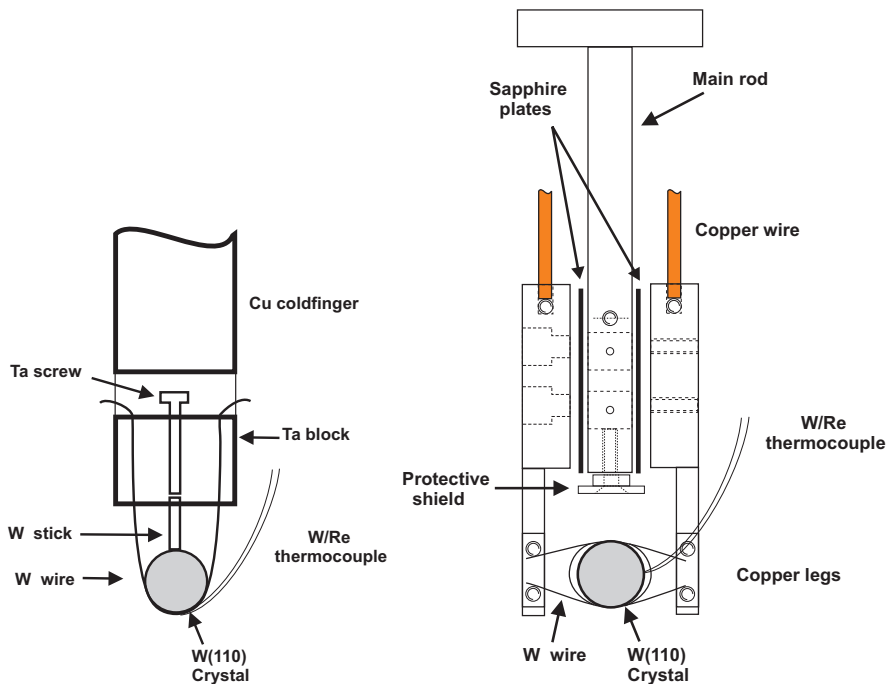
Figure 4.5: Left: the sample holder used in the early stage of this work. **Right**: exploded view of the actual sample holder.

15-20 A are used to obtain temperature above 1200 K. In the case of indirect heating, the electrons produced by a 5 A current flowing through the filament, are accelerated by +700 V voltage applied between sample and ground. The high temperatures required for flashing are obtained with the latter method.

For temperature measurement, an appropriate sensor should be used taking into account the wide temperature range, i.e. from 20 K to 2600 K in which the setup is operated. The only available tool covering such a temperature region is W/Re (W5%Re/W26%Re) type C thermocouple. This is installed in a 0.3 mm hole made in the W crystal, and is mounted uninterrupted from sample to thermovoltage display (Keithley 2000 multimeter) through a UHV flange where is glued. Thus, unwanted additional junctions are avoided and a better accuracy in temperature reading is obtained. This is very important in the low temperature range where the W/Re thermopower variations with temperature are very small. This can be seen in the left panel of figure 4.6, where the temperature variation between 20 K and 100 K corresponds to a thermovoltage value of $\approx 200 \mu V$. A step forward in improving the temperature accuracy was made using a electronic ice reference point (Newport) instead having the reference junction in an ice bath. The latter one can exhibits temperature gradients in the ice-water mixture, that can influence the temperature reading in an uncontrollable way. Even with this precautions, the measured thermovoltage can be influenced by a series of factors, which introduce errors in temperature reading *e.g.* bad contact sample - sensor. Thus, after each sample mounting a temperature calibration procedure has been done. In the low temperature range the calibration has been made
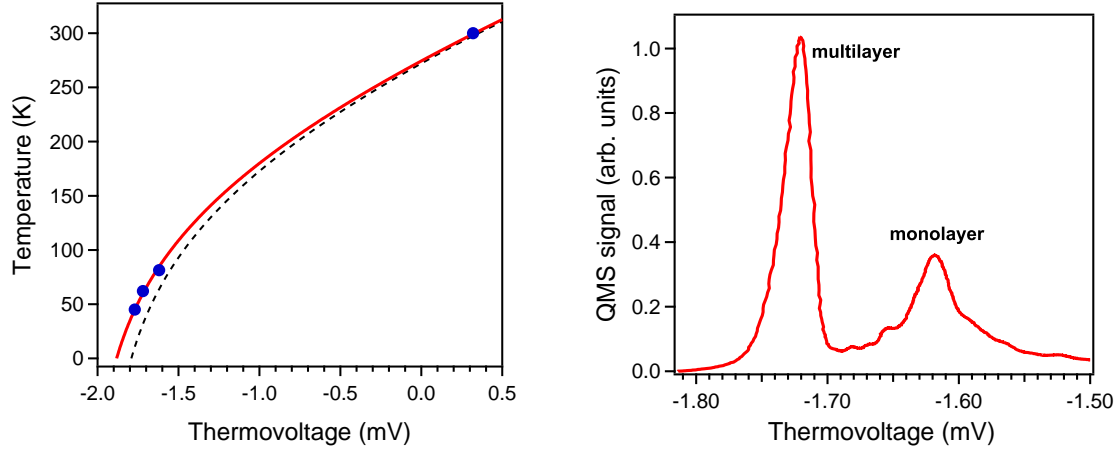
Figure 4.6: Calibration of the temperature reading of the W/Re thermocouple using TDS measurements from the W(110) substrate **Left**: Variations of the W/Re thermovoltage with temperature: the tabulated values (dashed line) together with the measured TDS desorption temperatures for Xe and O_2 (dots) used to obtain the calibration curve (solid line). Both curves are described by a fifth order polynomial. **Right**: typical TDS spectrum of Xe from W(110) substrate, showing the multilayer (low temperature) and the monolayer (higher temperature) desorption peaks.

employing thermal desorption spectroscopy, by using the measured desorption temperatures of physisorbed O_2 and Xe on W(110) sample. An exemplary TDS spectrum of the thermally desorbed Xe from the W(110) substrate is shown in the right panel of the figure 4.6. From here one can deduce the desorption temperatures (actually the measured thermovoltage) for the monolayer and the multilayer coverage of Xe. The same procedure is done also for the O_2. By comparing the measured desorption temperatures with the literature data one can get an estimation about the encountered deviation from the real temperature. Thus, the three low temperature points together with the room temperature point are used for the determination of the calibration curve (solid curve in fig. 4.6 left) employing the same polynomial fit function utilized to fit the tabulated values of thermovoltage vs. temperature for the W/Re thermocouple (dashed curve in fig. 4.6 left). From here an error in the temperature reading $\leq$10K is estimated. In the high temperatures (above $600°C$) region a pyrometer has been utilized.

4.2 Laser system

As mentioned earlier in this section, we use as a light source for the static and time-resolved linear and nonlinear optical measurements a home-made Titanium:sapphire (Ti:Al_2O_3) oscillator. There are two regimes in which the laser can be used:

1. the normal oscillator mode
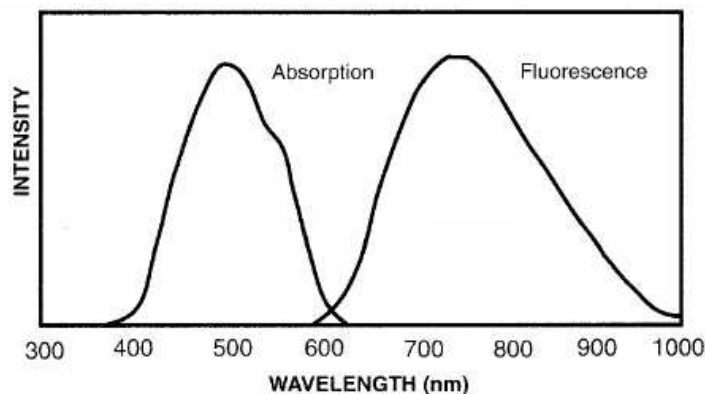
2. the cavity dumping mode

Figure 4.7: Absorption and emission (fluorescence) spectra of Ti:Sa crystal as a function of wavelength. Maximum in the Ti:Sa absorption (514 nm) is close to the wavelength of Nd:YVO$_3$ pump laser (532 nm). The broad bandwidth of the fluorescence spectrum supports the generation of ultrashort laser pulses. From [126].

In the normal oscillator regime, the typical operating parameters are: pulse energy around 6 nJ at a repetition rate of 76 MHz and thus an average power of 500 mW. In the cavity-dumping mode, the pulse energies are increased by almost an order of magnitude to $\sim$42 nJ at an adjustable repetition rate controlled by the cavity dumper control unit. For both regimes, pulses as short as 35 fs are delivered. Due to the higher pulse energy and the possibility of having a variable repetition rate, the cavity dumping variant has been chosen for all time-resolved measurements presented here. For some of the static measurements and the MSHG phase determination (see chapter 5) the oscillator variant has been employed. In the following, a short introduction in the theory of the femtosecond laser pulse generation and mode-locking technique is given, followed by the description of cavity-dump working mode of the oscillator.

4.2.1 Ultrashort laser pulse generation

Titanium doped Al$_2$O$_3$ crystal as an active laser medium presents several advantages, which makes it a very feasible choice in the construction of nowadays ultrafast lasers. First of all it exhibits a broadband gain/emission spectrum centered at 790 nm (see figure 4.7) and therefore having the capability to produce ultrashort (femtosecond) laser pulses. Generally, the laser pulse duration τ_p is determined by the time-bandwidth product $\Delta\nu \cdot \tau_p \geq C$, where $\Delta\nu$ represents the spectral bandwidth and C a constant factor that depends on the pulse profile *e.g.* C=0.441 for a gaussian pulse. Thus broader the spectral profile shorter is the laser pulse. Also, the excellent thermal properties and hardness makes from Ti:Sapphire the most utilized solid state laser material in building femtosecond laser oscillators and amplified laser systems.

The pulsed operation of Ti:Sa laser is obtained by means of the so-called *mode-locking* technique. This describes the operation of the laser with all the resonator frequency modes
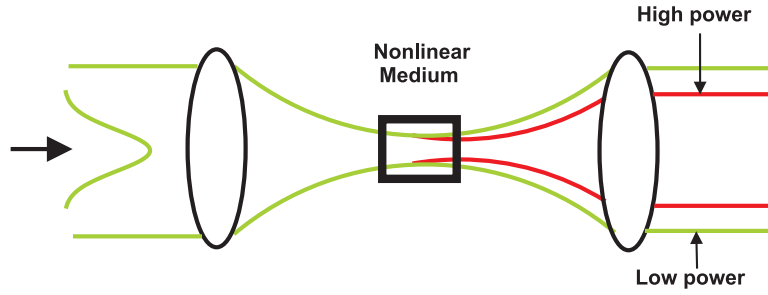
Figure 4.8: Illustration of the optical Kerr effect in the soft-aperture type of mode locking. The Kerr medium acts as a lens on the focused laser beam, producing a selective amplification of the higher intensity modes. These ones experience a bigger gain than the lower ones having the largest overlap with the excited gain medium.

phase locked (under the gain envelope). As a competing regime is continuous wave (CW) mode, when exists a arbitrary phase among the cavity modes. Mode locking is achieved through the *nonlinear optical Kerr effect* which produces the

- self focusing

- self-phase modulation

of the pump laser intracavity mode in the Ti:Sa crystal. This is due to dependence, in the high intensity regime, of the refractive index on the intensity according to the following relation:

$$n(\omega, t) = n_0(\omega) + n_2 I(\omega, t) \tag{4.1}$$

with $n_2 \sim \chi^{(3)}$ where n_0 and n_2 are the normal (complex) and the nonlinear part of refractive index, respectively, while $\chi^{(3)}$ is the third-order nonlinear susceptibility tensor that describe the bulk optical properties of the crystal (see chapter 3).

How the self focusing works is illustrated in the figure 4.8. As it travels through the nonlinear medium with a n_2 positive, the gaussian shaped laser pulse *i.e.* higher intensities in center then at the edges, encounters regions with different refractive index, which focus the beam being similar to a lens (Kerr-lens effect). Thus, the stronger intensity modes will experience a stronger focusing than the weaker ones which implicitly results in lower amount of losses for the former ones. This together with the insertion of a variable aperture in the cavity, suppress the weak intensity modes and the competing CW mode. This method is known as hard-aperture mode locking. The intrinsic character of self-focusing can be used for mode-locking without introducing any additional element in the laser cavity. The excited region of the gain medium forms by itself an "aperture" determined by spatial variation of the refractive index across the incident gaussian wavefront. Using this property one can initiate ML operation of the laser, this method being known as soft-aperture mode locking. The construction of the oscillator used in this work is based on the latter mentioned type of mode locking.

Beside the self-induced spatial variation of the refractive index *i.e.* self-focusing, there is also a variation in time due to the temporal distribution of the intensity in an ultrashort
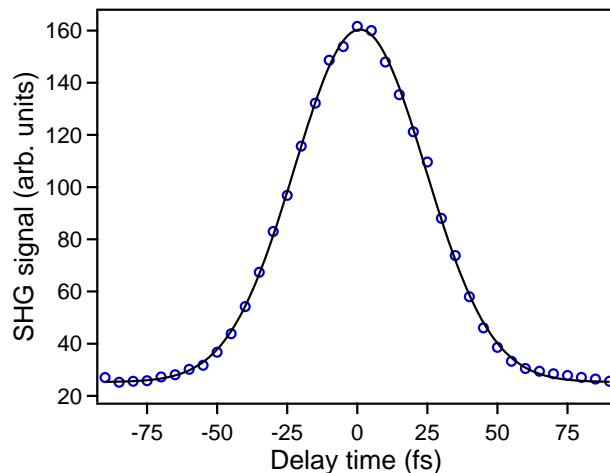
Figure 4.9: The cross-correlation signal (dots) between the pump and probe pulses measured on the gadolinium sample. Fitting (solid line) the CC curve with a gaussian one obtains a pulse duration of 33 fs.

laser pulse. This produces a change in the phase of the electric field of the pulse in a similar manner as in the aforementioned self-focusing: distribution in the intensity at the leading and the falling edge of the pulse results in the appearance of new frequency components in the pulse *i.e.* a chirped pulse. This is equivalent to a broader spectral width of the pulse that gives the possibility of generation of even shorter laser pulses. The ultimate pulse duration is given by the subtle interplay of the above mentioned phenomena with the group velocity dispersion (GVD), this point being discussed in the next paragraph.

Hence, the intensity dependent losses in the laser medium give rise to the initial build up of the pulsed regime. But the steady state operation of the laser depends on a series of factors. Generally speaking, the laser pulse duration is determined by the competition between group velocity dispersion and the quality of self-focusing in laser cavity. Taking into account the large emission bandwidth (according to the figure 4.7) of the Ti:Sapphire medium and the time-bandwidth product, pulses of 4 fs duration could be generated. But the positive GVD encountered by the laser pulse while is travels in the resonator, makes the pulse much longer. This limitation can be compensated, to some extent, by introducing in laser cavity optical components producing a negative GVD *e.g.* a prism compressor. Depending on the prisms material the compensation of positive GVD can be make up to second order dispersion term. Higher orders dispersion can be compensated by using chirped mirrors. Hence, having the prims as an active control over GVD delay is possible to generate pulses as short as 10 fs. With the actual oscillator configuration pulses around 35 fs are produced as can be deduced from cross-correlation curves measured directly on the sample (see figure 4.9).
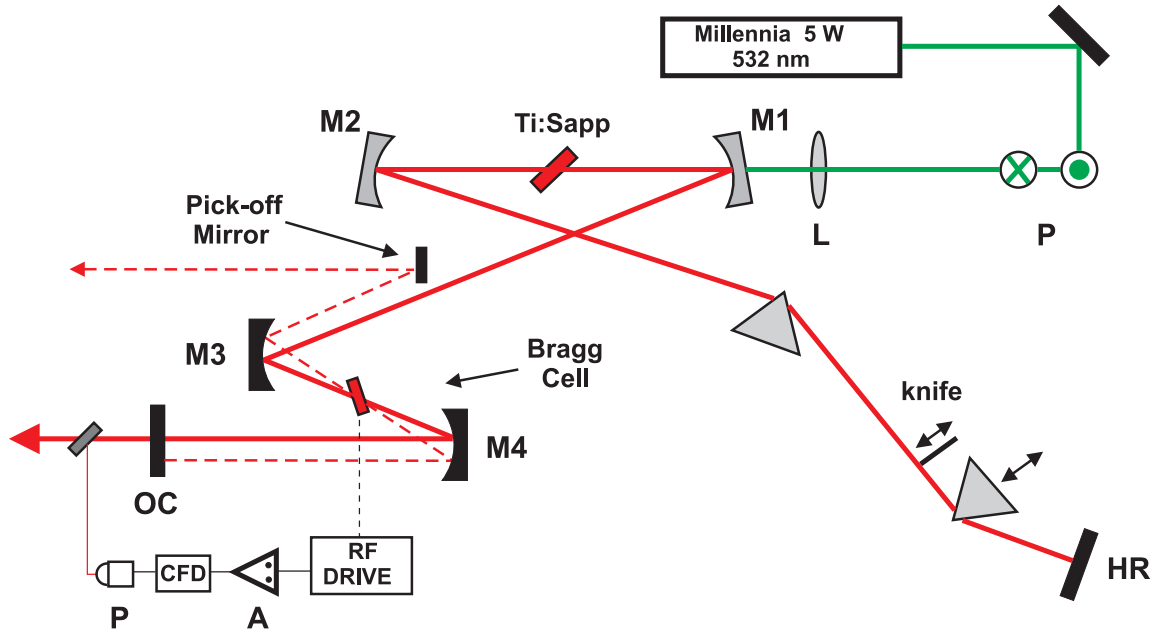
Figure 4.10: The layout of the Ti:Sa oscillator: Nd:YVO$_3$ pump laser (Millennia); P periscope; L anti-reflection coated focusing lens; M$_1$ and M$_2$ spherical mirrors; Ti:Sapp titanium sapphire crystal; HR high reflective end mirror; M$_3$ and M$_4$ curved mirrors enclosing the Bragg cell; OC output coupler; P photodiode, A amplifier, constant fraction discriminator and the cavity dumper control (RF Drive) unit forming the feedback circuit for the cavity-dump regime. Note, that the diffracted beam from the Bragg cell is deflected vertically, although is depicted (for clarity) as being in the plane of the figure.

4.2.2 Cavity-dumped Titanium:Sapphire oscillator

The cavity-dump version of the Ti:Sapphire laser is an intermediate solution between the high repetition rate but low pulse energies delivered by oscillators ($\approx$80 MHz repetition rate and few nJ pulse energy) and the amplified systems with variable repetition rate and high peak powers (hundreds of KHz repetition rate and pulse energy in the mJ range). This cavity-dump variant is well suited for nonlinear optical experiments and in general for time-resolved experiments because it provides ultrashort laser pulses at a variable repetition rate with a medium pulse energy and more important keeping the thermal load of the sample at insignificant levels. The cavity dump version of the Ti:Sa oscillator used in this work is schematically illustrated in the figure 4.10.

The oscillator is constructed in a X configuration with two asymmetric length branches. For pumping the Ti:Sa crystal, the second-harmonic (532 nm) of a diode laser (Millennia 5W, Spectra Physics) is used, which is coupled into the oscillator via a periscope. This serves also as a polarization rotation device, the output pump laser polarization being perpendicular to the plane of laser table. The CW pump beam is focused on to the Ti:Sa crystal, which is Brewster-oriented for minimizing the losses due to reflection. The optical resonator comprises six mirrors: two spherical mirrors around the Ti:Sa crystal, that
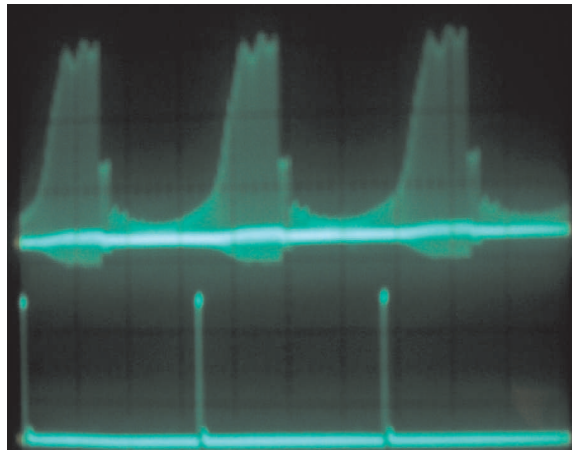
Figure 4.11: Cavity dump pulse train at a repetition rate of 1,52 MHz (upper part) together with the original pulse (lower part) at a repetition rate of 76 MHz as monitored by a fast photodiode placed outside the laser cavity (see fig. 4.10).

are highly transmissive for pump light (532 nm) and highly reflective for laser radiation centered at 800 nm; another two high reflective (HR) mirrors enclose the cavity with one of them acting as an output coupler (OC). Depending on the used configuration *i.e.* cavity dumping or normal oscillator regime the OC transmission has been 4% or 10%, respectively. In addition, two curved mirrors are inserted in the shorter arm which form the Bragg cell together with a fused silica crystal. The dumped pulse train is deflected out of the oscillator by the pick-off mirror. In the longer arm a combination of two fused silica prims mounted in a double-pass configuration are installed for GVD compensation. This material possess a small third order dispersion therefore having a small contribution to the pulse broadening. A knife is inserted before the second prism in order to tune the laser wavelength. The residual light reflected from the knife detected by a photodiode, is used to monitor (with an oscilloscope) the pulse train in the oscillator.

The mode-locking regime is initiated by slightly tapping the high reflective mirror, that encloses the oscillator cavity. This can be done also by moving back and forth the prism in the laser beam at the dispersive branch of the resonator. In order to improve stability of the laser running in the mode-locked regime, the oscillator is covered with a plastic box, which stops any air flow and dust particles to enter in the laser cavity.

Coming back to the cavity dumper regime, the underlying physical principle is the diffraction of laser light from an acoustically induced optical grating *i.e.* spatially modulation of the refractive index in the crystal. The acoustic wave is produced by a piezoelectric transducer attached at the bottom of the fused silica crystal. For this regime an output coupler with 4% transmission has been installed, which decreases the losses compared to the normal oscillator mode (a 10% OC is used) and thereby increasing the amount of energy stored in the cavity. By switching on and off the high frequency acoustical wave, the first order diffracted pulse train is coupled out of the cavity. An example of such dumped pulse train is presented in the figure 4.11.

With this method the pulse energy could be increased by roughly one order of magnitude with little effect on the pulse duration. Without the Bragg cell installed in the laser cavity, the oscillator could deliver pulses around 25 fs duration [127]. In principle, additional dispersion introduced by the Bragg cell can be compensated by increasing the separation length between prisms or using chirped mirrors. However, the 35 fs pulse duration is enough for the purposes of the present thesis. The cavity dumper regime has been implemented with the help of the above mentioned Bragg cell controlled electronically by a driving unit (APE Berlin). This one is synchronized at the repetition rate of the laser, being triggered by the signal of a fast photodiode. In the feed-back circuit an amplifier and a constant fraction discriminator are employed due to the low signal level during dumping and that keep a clean triggering signal. The jitter of control unit is smaller than 50 ps with an electronic rise/fall time around 2 ns which is small compared to round trip in the oscillator 13 ns. Variable dumping repetition rates in the range of 1:20 to 1:5000 with regard to seeding laser frequency are available with the present setup. Similar diffraction efficiencies were obtained with the 1:50 and 1:100 ratios, which have been used in this work. These two ratios that correspond to 1.52 MHz and 760 KHz repetition rates, respectively, have been selected since they provide a high pulse energy with a negligible thermal load of the sample and, very important, a stable operating regime of the oscillator. For more technical details about the oscillator construction the reader is referred to Uwe Conrad's thesis [127].

4.3 Pump-probe scheme for TR measurements

The layout of the optical pump-probe scheme together with the laser beam paths on the laser table, in the UHV chamber and in the detection block are depicted in the figure 4.12. The UHV chamber is installed near by the laser table.

At the exit from the oscillator a second prism compressor is installed for compensating any additional GVD acquired along the optical path from oscillator to the sample *e.g.* air, mirrors, UHV window. The prisms are made of SF11 material which provide, in a double-pass path, a negative GVD in order of -4550 fs^2 [127]. Here, a reference channel detecting the SHG signal from a nonlinear crystal is installed, in order to monitor the fluctuations in the laser intensity. It consists of a beam splitter, lens, beta barium borate (BBO) crystal and a photodiode. A small part of the laser output is reflected by the beam splitter onto the lens and focused in the BBO crystal, that produces SHG in transmission which is detected by the photodiode.

The layout of the pump-probe scheme is shown in figure 4.12: after a beam splitter which separates the pump and probe beams in a 4:1 ratio, the pump beam is delayed with respect to probe by a delay stage (Physik Instruments). The smallest delay step is 0.5 fs. A chopper working at a frequency of 700 Hz, is inserted in the pump beam that makes possible to measure pump-induced variations of the detected signal *i.e.* to measure the probe signal for on and off pump. From here, both beams are directed to the UHV chamber in a collinear manner and focused on the sample using a plano-convex lens (fused silica f=100 mm). For a better focusing condition a special flange has been designed, which allows positioning of the focusing lens very close to the sample. Hence, a
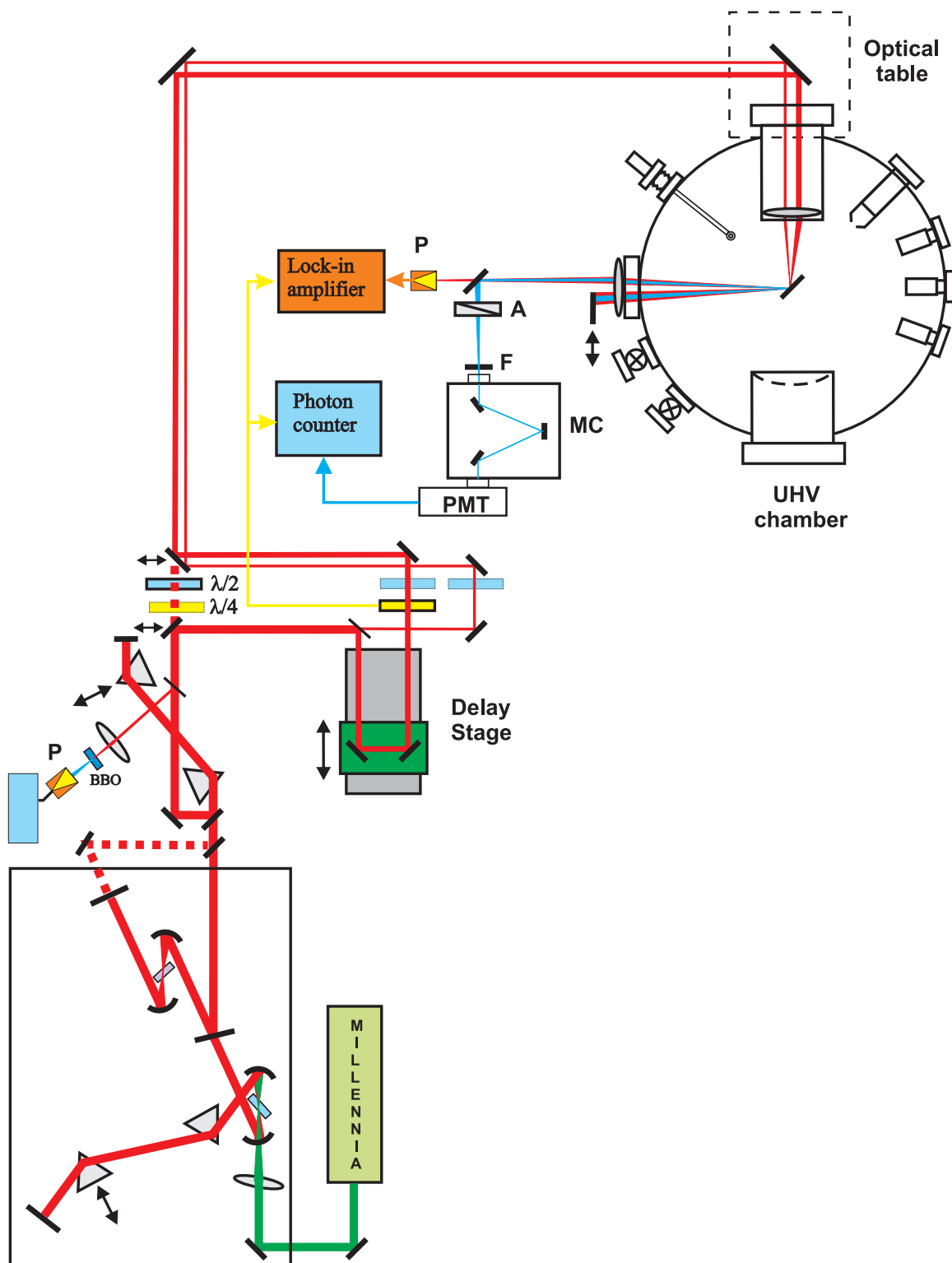
Figure 4.12: General view of the optical setup on the laser table. In the lower part the laser oscillator together with the reference channel (P-photodiode, BBO nonlinear crystal), prisms compressor and the pump-probe scheme, while in the upper part the beams path ($\lambda/2$ half-wave plate, $\lambda/4$ quarter-wave plate) in the UHV chamber and in the detection block (P-photodiode, A-analyzer, F-filter, M-monochromator, PMT-photomultiplier tube) are depicted.
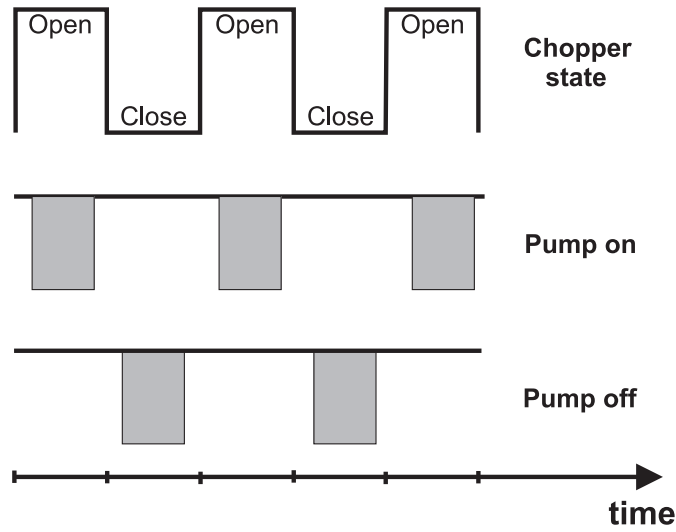
Figure 4.13: The open and close chopper states are schematically depicted and the corresponding measured signal for pump on and off. The divisions on the time axis correspond to $1/\mathrm{f}_{chopper}$ where $\mathrm{f}_{chopper}$ denotes the chopper frequency.

bigger laser fluence is obtainable: $\sim 0.9 mJ/cm^2$ for a focus diameter of ~ 70 μm and a pump pulse energy of 34 nJ. The focus quality and the position of the laser beams on the sample is checked with a microscope and a CCD (charge coupled devices) camera. This imaging part is used also for the spatial overlap of pump and probe beams on the sample. At this point is worthwhile mentioning the way of determination of the beam diameter in focus. Due to the actual configuration of the setup we had to measure the focused beam diameter on the laser table by using the sliding knife-edge technique [128]. The laser optical path to the sample has been mimic by using the same focusing lens and the same type of UHV window as in the real setup. For the single-beam scheme the obtained beam diameter is $\approx 52\mu$m while for the pump-probe scheme a diameter of $\approx 70\mu$m has been deduced. The last result is presumably due to the fact that the collinear pump and probe beams are incident on the focusing lens in off-centered positions and thus a less efficient focusing condition is encountered. Hence the resulting laser fluences for the single-beam and pump-probe schemes are $\sim 2mJ/cm^2$ and $\sim 0.9mJ/cm^2$, respectively.

A stable and flexible optical table has been made, that is attached to the UHV chamber, on which the mirror that directs the beams to the chamber and the focussing lens are mounted (typically). Due to its design the optical table offers a higher degree of freedom in collimating and focusing the laser onto the sample, allowing various optical items and optical schemes (*e.g.* SHG phase measurement in chapter 5) to be installed. After hitting the sample at 45° incidence angle, the beams are collimated and directed to the detection part. Note, that the entrance and exit UHV windows are made of fused silica since this material exhibits a high transmittance coefficient ($\geq 95\%$) from UV throughout the visible spectral range and do not produce any residual SHG signal.

For polarization dependent measurements, and in general for changing the polarization of

the incident beams, a $\lambda/2$ half-wave plate is used (yellow rectangle in figure 4.12) or/and a $\lambda/4$ quarter-wave plate. In the detection block, a Glan-Taylor polarizer is used as an analyzer of the output SHG polarization.

The detection scheme consists of two branches: one is detecting the linear reflectivity *i.e.* at fundamental wavelength 800 nm (typical) and another one detecting the second harmonic (400 nm) signal. The linear reflectivity is recorded with the help of a photodiode and a lock-in amplifier whereas the SH reflectivity is measured with a photomultiplier and a photon counter. Both, the lock-in and the photon counter, are synchronized with the chopper (see fig. 4.12). The fundamental and the SH beams reflected-off the sample are separated with a dichroic mirror. For time resolved measurements, the pump and the cross-correlation signals are closed with a knife mounted on a translation stage (see figure 4.14). This can be done for both, fundamental and SHG signal, since they are reflected in a collinear geometry.

The SH signal from the sample is detected in the single photon counting mode due to the relatively low SHG efficiency from the gadolinium films. Owing to the relatively low SHG yield from Gd and Y surfaces, a special care is devoted to eliminate the potential noise in the measurement. Hence, spectral filtering and low noise level are obtained by using a monochromator together with a thick (2 mm) BK39 filter. Also the photomultiplier (R4220P Hamamatsu) has a spectral response centered at 410 nm and several orders of magnitude smaller sensitivity for 800 nm *i.e.* fundamental wavelength. As an additional way to avoid any environmental stray light to enter in the detection block, the whole optical scheme (together with the oscillator and the UHV chamber) is installed under a light protective tent.

The photocurrent generated by the SH photons in the photomultiplier (quantum efficiency of around 23% at 400 nm) is subsequently amplified and fed into the photon counter. Here, the signal is measured in two channels corresponding to "on" and "off" chopper phase. This is illustrated in the figure 4.13.

For a pump-probe measurement, opening and closing the chopper is equivalent to the detection of the probe signal for positive and negative delays, respectively (assuming chopper in the pump and the pump and the cross-correlation signal suppressed). In the case of a static measurement, during the "on" phase the signal plus noise is detected while for "off" phase just the noise is measured. Additional substraction of the signal measured in the two channels, remove the noise (mainly environmental) measured in the dark phase of the chopper.

A relatively similar measurement procedure is used to detect the pump-induced variations in linear reflectivity. The reflected probe beam is incident onto silicon photodiode (BPX61 Siemens) and the produced photocurrent is feed into a specially designed amplification stage. This one allows a simultaneous detection of the time-integrated (R_0) and time-modulated ΔR linear reflectivity signal. With this setup we can resolve relative variations in the transient linear reflectivity $\Delta R/R_0$ down to 1×10^{-5}.

The entire setup is remotely controlled by a computer under a LabView programming environment. The instruments are interconnected in a GPIB (General Purpose Interface Bus) driven circuit. The LabView environment has been implemented during this work, which increases the data acquisition speed and ensures an efficient data-collection and
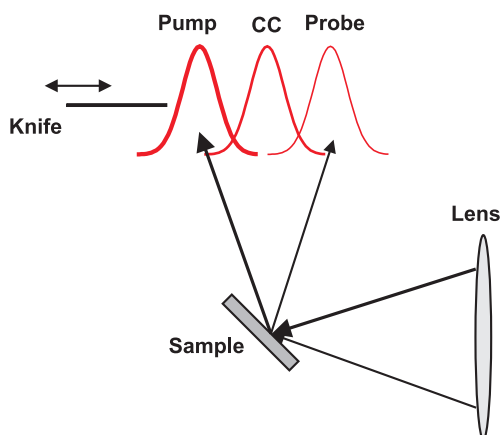
Figure 4.14: Schematic description of the detection geometry in the pump-probe scheme: the pump and probe beams are focussed on the sample and in reflection one can distinguish, assuming that the pump and probe are overlapped in space and time, the SHG signal coming from the pump, probe and the cross-correlation (CC) beams. These beams are denoted in the figure as having gaussian profile. For a time-resolved measurement the pump and the cross-correlation signal are blocked with the knife, only the probe signal being detected.

averaging. Therefore, the statistics in measured data has been sensitively improved, a fact that is very important for demanding measurements with an increased level of noise due to variation of an external parameter *e.g.* the temperature-dependent data in chapter 5. Also, for the temperature-dependent measurements and generally for the annealing procedure and running temperature ramps in the TDS measurements, a PID (Proportional Integral Differential) software has been developed. By this, an accuracy in temperature stabilization of $\pm$ 1 K in the low temperature range and $\pm$ 0.1 K at higher temperatures is obtained.

4.4 Measurement description

At the end of this experimental chapter, a day-by-day measurement workflow is described as is relevant for an interested reader and for getting a better understanding regarding the entire experimental setup.

After the Gd(0001) thin film is deposited and annealed, the crystalline quality is checked with LEED. The next step is to align the oscillator, first getting the optimal output power in CW mode and afterwards in the mode-locked mode. The laser wavelength is tuned and the spectral shape of the pulse is displayed with the help of CCD spectrometer and the PC monitor. In the case that one runs the oscillator in cavity-dump regime, the pick-off mirror is slightly inserted in the laser beam. Running a cw acoustical wave through the fused silica crystal in the Bragg cell, one can mimic the normal CD regime, and by this the output power can be checked. The power is optimized by changing the z position, the rotation coordinate and the tilting angle of the Bragg crystal, trying to get the maximum power and in the same time a stable laser regime. Afterwards, a more fine adjustment is done by varying the parameters of cavity-dumper control unit *i.e.* phase, delay, acoustical pulse width.

In the next stage, the alignment of the external compressor is done, which is made by positioning the laser beam on the standard height (pinhole like) plates, and keeping the beams at the very edge of the prisms in order to get as small as possible the positive GVD. In case of a time-resolved measurement, the pump-probe scheme is employed by inserting a pair of mirrors in the laser beam path, and the shape and parallelism of pump

and probe beams are verified. After this, the beams are guided to the UHV chamber from where are focussed onto the sample. Focussing is made with the entrance lens, mounted on a special holder which allows movement in x, y, and z directions. The reflected beam from the sample is adjusted in the detection block by rotating the sample and optimizing the position of the collimating lens. The position and the overlap of the beams on the sample are checked with the microscope and the CCD camera. The photon counter and the high-voltage power supply of the photomultiplier are turned on, and the SHG signal level is measured in the two channels, which correspond to pump on/off or signal+noise and dark-phase noise (see preceding section) for the one-beam scheme. The probe signal is optimized by moving the focusing lens and also adjusting the prisms position in the external compressor, that compensate the positive GVD. After this, the pump signal is closed with the knife and the cross-correlation signal is optimized by overlapping the pump and probe beams on the sample. At this point, the CC curve is measured and the zero time delay between the pump and probe pulses is checked and eventually modified. After the zero delay is set, the CC signal is also closed, the photon counter measuring just the probe signal for open and closed pump. The last point is to optimize the signal from photodiode, that measures linear reflectivity. After all this sequential steps have been performed, one can starts the time-resolved (static) SHG and LR measurements.